Hydraulically actuated micro-contact printing engines



2011 J. Micromech. Microeng. 21 085013

(http://iopscience.iop.org/0960-1317/21/8/085013)

J. Micromech. Microeng. **21** (2011) 085013 (10pp) doi:10.1088/0960-1317/21/8/085013

# Hydraulically actuated micro-contact printing engines

**K Choonee**[1] **and R R A Syms**

EEE Department, Imperial College London, Exhibition Road, London SW7 2AZ, UK

E-mail: kaushal.choonee@imperial.ac.uk

Received 21 February 2011, in final form 23 May 2011
Published 30 June 2011
Online at stacks.iop.org/JMM/21/085013

**Abstract**

Micro-contact printing ($\mu$CP) is a rapid, simple and well-established method of microscale biochemical patterning. However, there is a lack of inexpensive and accessible tools for accurately controlling contact during the printing process. In this paper, controlled $\mu$CP using hydraulic actuation is demonstrated. Complete printing systems, including a substrate placed at a calibrated height above an elastic stamp attached to a hydraulic chuck, are constructed and characterized. The chucks are made from Perspex using precision machining while the stamp is made by casting against microfabricated silicon masters. The total patterned area is $\sim$25 mm$^2$ and 10 $\mu$m wide features have been printed.

(Some figures in this article are in colour only in the electronic version)

## 1. Introduction

Micro-contact printing ($\mu$CP) is a simple method of patterning surfaces at the microscale and was first introduced in 1993 by Kumar and Whitesides [1]. The process involves coating a stamp carrying features with ink and pressing it against a substrate. Typically, the stamp is made of the elastomer poly(dimethyl)siloxane (PDMS) while the ink and substrate are an alkanethiol and Au, respectively. The alkanethiols form self-assembled monolayers (SAM) on Au and can be used as a mask for a subsequent etch or as a template for further growth or assembly. The $\mu$CP process and some of its applications are summarized in [2]. In addition to alkanethiols on gold, a number of compatible ink/substrate combinations are possible and some reviews can be found in [3, 4].

Although initially intended as an alternative to photolithography [2], $\mu$CP is finding more interest in the field of biochemistry [5] where it enables the control of surface properties at the microscale. In addition, $\mu$CP does not involve changes in pH or temperature and is one of the few methods of biomolecule patterning that has been shown to retain biochemical functionality; e.g. in [6], protein layers were successfully deposited onto a substrate without loss of activity.

The stamp material, PDMS, has several characteristics which are critical to $\mu$CP. Firstly, it is cheap, easy to machine by casting and moulding, and therefore accessible. It is homogeneous, isotropic, optically transparent, provides a surface with low interfacial free energy and is chemically inert [2]. It is porous and has a tendency to adsorb certain molecules [7], which is advantageous for $\mu$CP. Its chemical properties can also be tailored for specific applications, e.g. by exposing it to oxygen plasma [8, 9]. The plasma treatment can also be used to irreversibly bind PDMS surfaces to glass or to each other [10–12] and hence enables the construction of complex 3D geometries.

The low stiffness of PDMS (Young's modulus 1–2 MPa), whilst allowing conformal contact over large areas, is also a limitation as the features on the stamp tend to get distorted. In practice, the aspect ratio of relief features on the stamp are limited to 0.2–2 [13] to generate defect free patterns. Improved PDMS formulations [14] and tri-layer stamps [14, 15] solve this issue to some extent. However, for repeatable and accurate $\mu$CP, controlled loading is required to ensure conformal contact without excessive distortion of the features. As substrate areas are increased, trapped air pockets, which lead to further distortion, become problematic as well. One solution is a stamp aligner which presses a glass-backed stamp against a substrate under vacuum [16]. Another involves a flexible stamp held in a bent state above a substrate and gradually released to contact the substrate [17]. A further ingenuous method involves a PDMS stamp mounted onto an array of grooves, which can

[1] Author to whom any correspondence should be addressed.

 

individually be switched from vacuum to mild pressure, and thus allow controlled actuation of small sections of the stamp at a time, rather than the entire stamp. This has been shown to minimize pattern distortion [18]. Whilst these methods are successful, they require complex proximity aligners and are thus often inaccessible to non-silicon end-users such as biochemists.

Accessible systems such as customized systems that combine three-axis alignment with an optical microscope have been developed [19] and have been used to bind neurons to metallic electrodes. Similar systems including controlled loading with a linear pneumatic actuator [20] or a diaphragm-like stamp driven by compressed air [21] have also been developed. Recently, complete $\mu$CP print engines made using micro-electromechanical systems (MEMS) technology have been proposed [22]. Whilst this approach successfully combines the alignment, flexure and stamp into a single miniature engine, controlled loading by electrostatic actuation has been shown to be problematic and prone to discharge. In fact, all successful $\mu$CP systems with controlled loading encountered so far are based on pneumatic actuation.

This is hardly surprising as fluidic (pneumatic or hydraulic) micro-actuators can deliver high force and power densities at the microscale in comparison to electrostatic, thermal or piezo-electric actuators [23]. Despite this property, this class of actuators is often overlooked in MEMS, and applications are more common in micro-fluidics and micro-total-analysis systems. For example, numerous pneumatically operated valves and pumps have been developed and some examples are reviewed by Oh *et al* [24] and Laser *et al* [25], respectively. The most common form of fluidic actuators is membrane-like pneumatic actuators [23] due partly to their ease of fabrication. Silicone rubber such as PDMS is very popular in such applications because of its low stiffness, which implies large deflections under small loads. Examples of such actuators include a refreshable Braille cell array actuated with compressed air [26], a tuneable elastomeric mould whose shape is adjusted pneumatically [27], and various other components for micro-fluidic systems as summarized in [28].

Hydraulic actuation in MEMS, on the other hand, is much less common and not widely reported. The main difference between a hydraulic system and a pneumatic one is the type of fluid used and hence the input parameter that is controlled. The former uses an incompressible fluid such as water and hence the input is a calibrated injection volume, whilst the latter uses a readily compressible fluid such as air with the input parameter being pressure. With the input parameter being volume, operation can be easily controlled with benchtop syringe drivers that allow careful metering of the injection volume, thus making the complete $\mu$CP system truly accessible.

An issue with fluidic actuators is the interconnection of microscale components to the macro world, which is non-trivial. This is often a hurdle in micro-fluidics (and hence hydraulics), especially when a large number of connections are involved [29, 30], but a number of solutions in the form of pre-formed interconnecting ports exist and are described in [31, 32].

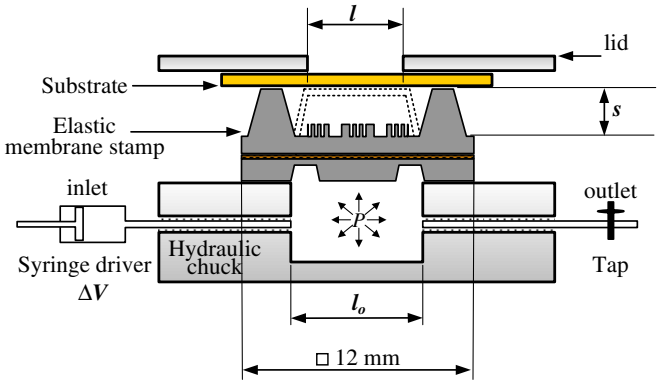


**Figure 1.** Schematic of the hydraulic $\mu$CP system. The substrate is held at a flying height, $s$, above the stamp. The distance $s$ is set by the spacer built into the stamp, and the substrate is held against the spacer through a lid which is clamped onto the hydraulic chuck (the clamps are not shown here).

In this paper, $\mu$CP driven by hydraulic actuation will be developed and characterized. The $\mu$CP engine will be made in a MEMS process as originally proposed by the authors in [33]. In the previous work, a replica-moulded stamp carrying self-alignment features, a flexure, an elastic backing and the print patterns was used to demonstrate six-level printing without the need for alignment optics. In this paper, a similar approach is adopted with regard to device fabrication and the focus is on adding further control on the printing process using a hydraulic actuation mechanism. Single-level controlled $\mu$CP is successfully demonstrated with this novel approach.

## 2. Design and concept

In this section, the hydraulically actuated $\mu$CP engine is described. The design is based on the replica-moulded stamp described in [33], and the operation of the modified design is verified through finite element analysis (FEA) and analytical models.

### 2.1. Hydraulic actuation

The main features of the proposed hydraulic system are illustrated in figure 1. It consists of a precision machined chuck with inlet and outlet pipes, and a square cavity of length $l_o = 8800$ $\mu$m, which is equal to the movable area of the $\mu$CP engine. An elastic deformable stamp seals off the cavity and deflects when controlled volumes of hydraulic fluid (water in this case) are injected with the syringe driver. Since water is practically incompressible (see e.g. [34]), the volume enclosed by the deformed stamp (illustrated by dotted lines) is equal to the injected volume, $\Delta V$. The outlet is closed off by a tap which can be opened for flushing the system or deflating the deformed membrane after actuation. By Pascal's principle, neglecting the height differences, the pressure throughout the closed system is constant and equal to $P$.

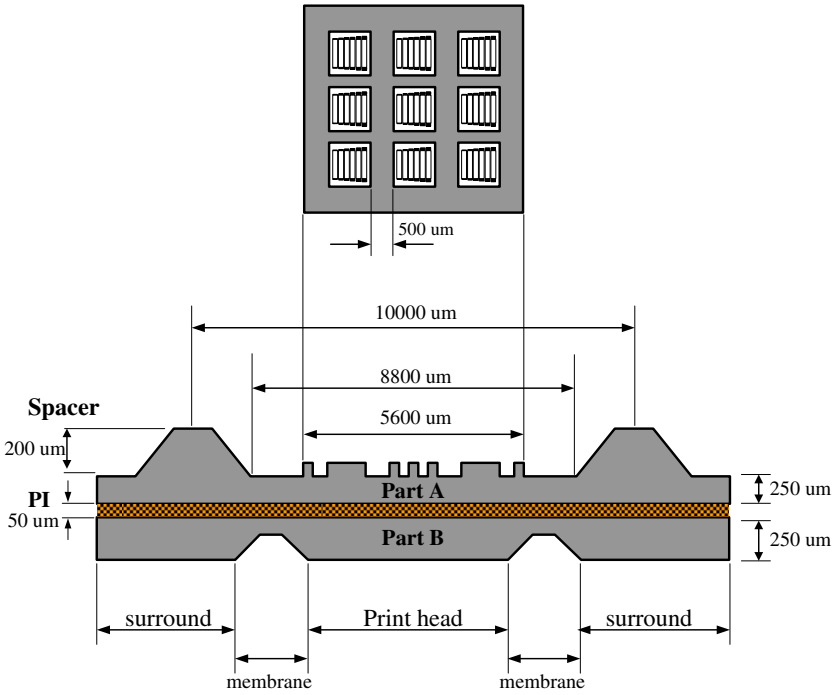


**Figure 2.** $\mu$CP engine with PI elastic backing. The lower schematic is a cross-sectional view highlighting how the print head is thicker whilst the membrane is thinner and allowed to deflect. The upper drawing shows a plan view of the print head and the 10 $\mu$m tall relief features which form the pattern. The pattern consists of 500 $\mu$m wide support bars that form a 3 × 3 array. Each element of the array carries 10 $\mu$m wide parallel bars with a period of 20 $\mu$m.

### *2.2. Replica-moulded $\mu$CP stamp*

The stamp is a tri-layer type consisting of a layer of 50 $\mu$m thick Kapton polyimide (PI) sheet sandwiched between two 250 $\mu$m thick PDMS parts. The overall structure contains a print head, a flexible membrane region, relief features to be printed, and spacers to set the flying height of the substrate. The stamp and its main dimensions are shown in figure 2. The relief features are 10 $\mu$m tall and contain 500 $\mu$m wide support bars as well as 10 $\mu$m wide parallel bars with a period of 20 $\mu$m, as illustrated in the plan view. Detailed fabrication steps are presented later, but briefly part A and part B are first spin cast and then cured on their silicon masters. The PI film is bonded to part B whilst it is still attached to the master. The PI–part B stack is peeled off, aligned to the print head of part A, and bonded together. Some misalignment between parts A and B is expected but this does not severely affect the performance of the printing operation since the PI film dominates the mechanical characteristics. Lastly, the tri-layer stamp is manually aligned to the precision machined chuck and attached with adhesive to form the system in figure 1.

### *2.3. Modelling of the membrane*

The mechanical behaviour of the hydraulic $\mu$CP is characterized firstly by simplifying the multi-layer membrane to a uniform structure with thickness-weighted properties, and using relevant analytical approximations to provide insight. This model is then verified by FEA of the full structure.

*2.3.1. Strain energy stored in bending.* The multi-layered replica-moulded stamp is first modelled as a single-layered homogeneous elastic membrane of Young's modulus $E_m$ and Poisson's ratio $\upsilon_m$. Using thickness-weighted average values, Young's modulus and Poisson's ratio can be expressed respectively as $E_m = (E_{\mathrm{PDMS}}h_{\mathrm{PDMS}} + E_{\mathrm{PI}}h_{\mathrm{PI}})/(h_{\mathrm{PDMS}} + h_{\mathrm{PI}})$ and $\upsilon_m = (\upsilon_{\mathrm{PDMS}}h_{\mathrm{PDMS}} + \upsilon_{\mathrm{PI}}h_{\mathrm{PI}})/(h_{\mathrm{PDMS}}+h_{\mathrm{PI}})$, where $h$ denotes the thickness and the subscripts denote the respective layers. The elastic constants for both materials in the multilayer structure are $E_{\mathrm{PDMS}} = 1\,\mathrm{MPa}$, $E_{\mathrm{PI}} = 2.5\,\mathrm{GPa}$, $\upsilon_{\mathrm{PDMS}} = 0.5$ and $\upsilon_{\mathrm{PI}} = 0.35$ [35]. Using $h_{\mathrm{PDMS}} = 500\,\mu\mathrm{m}$ and $h_{\mathrm{PI}} = 50\,\mu\mathrm{m}$, the average values are $E_m = 218\,\mathrm{MPa}$ and $\upsilon_m = 0.49$.

Following Timoshenko [36], an approximate solution to the large deflection of thin plates (i.e. deflections many times larger than their thickness) can be obtained from the energy method. For such thin plates, the resistance to bending can be neglected and the flexural rigidity $D = Eh^3/(12(1-\upsilon))$ can be taken to be zero. The strain energy is then due only to the stretching of the middle plane and can then be expressed solely in terms of tensile and shear strains in the $x$–$y$ plane, i.e. in the plane of the membrane (see equation (248) of [36]).

Assuming suitable expressions for the displacements on the membrane, and $\upsilon = 0.25$, the strain energy, $U$, of the membrane due to the stretching of its middle surface can be expressed as

$$U = Eh/7.5\big[5\pi^4 w_o^4/64a^2 - 17\pi^2 c w_o^2/6a + c^2(35\pi^2/4 + 80/9)\big]. \quad (1)$$

Here, $2a$ is the length of the square membrane, $c = 0.147w_o^2/a$, $w_o$ is the maximum deflection at the centre and $h$

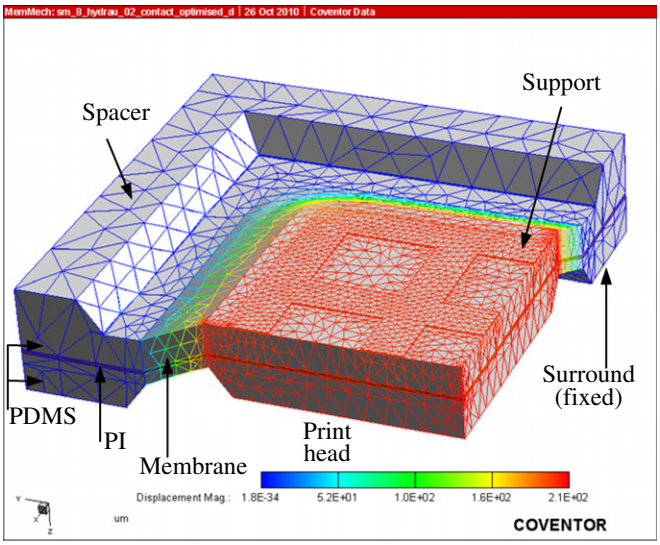


**Figure 3.** Model used for finite element simulation. The relevant surfaces/parts are labelled.

is the thickness of the membrane. Using equation (1) with $h = 550\ \mu$m and $E = E_m = 218$ MPa, the maximum displacements measured can be related to the strain energy in the membrane. Note that this expression assumes $\nu = 0.25$, whilst the actual value $\nu_m = 0.49$. In the case of large deflection of a membrane, the energy is weakly dependent on the Poisson ratio (see e.g. [36, 37]) and hence equation (1) provides a reasonable approximation.

*2.3.2. Volume enclosed by the deformed membrane under contact.* The membrane after deformation and contact with a flat surface at a flying height $s$ is illustrated by the dotted line in figure 1. The membrane is assumed to deform to a trapezoidal shape, although the sloping edges are likely to be curved in reality. However, given the small value of $s$ (at most 200 $\mu$m) compared to the base ($l_o = 8800\ \mu$m), the volume under the sloping regions is negligible compared to the total volume enclosed.

The volume enclosed is thus approximated by the difference between two square-based pyramids, one with a base of length $l_o = 8800\ \mu$m, and height $d$, and the other of base length $l$, and height $(d-s)$. For $0 < l < 5600\ \mu$m, $d = sl_o/(l_o - l)$, and the volume enclosed is given by

$$\Delta V = 1/3\big(l_o^2 d - l^2(d-s)\big). \tag{2}$$

The normalized contact area is given by $(l/5600)^2$, where $l$ is in $\mu$m.

### 2.4. Simulation

The mechanical response of the stamp and the interaction with the substrate is investigated by FEA using the CoventorWare (CoventorWare 2008 Analyzer, Coventor Inc.) package. The steady-state operation is characterized using a mechanical solver by applying a uniform load to the surfaces of part B that are exposed to the hydraulic fluid and computing the deformation. Exploiting symmetry, only a quarter of the structure is simulated with appropriate boundary conditions

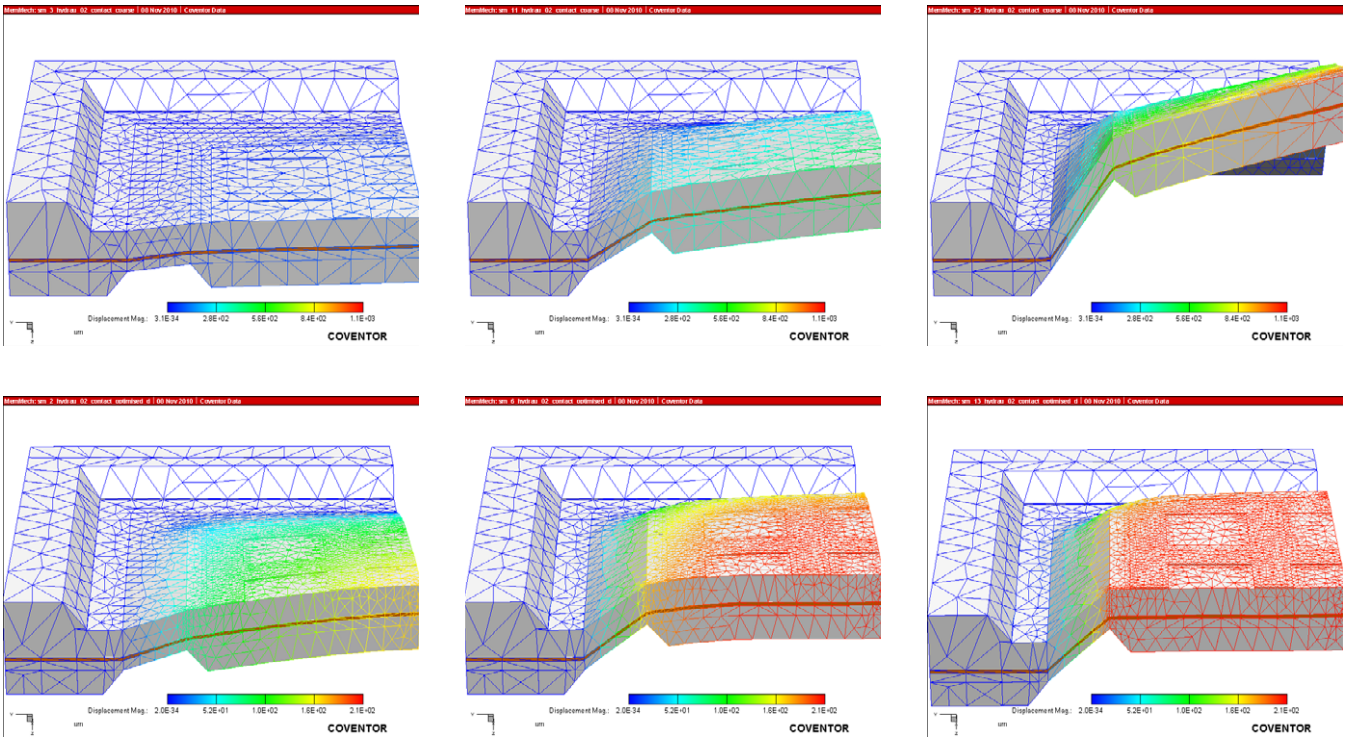


**Figure 4.** Upper row: deformation of the membrane without any contact surface. Lower row: deformation of the membrane with a contact surface 190 $\mu$m from the initial surface. Deformation in the bottom row is exaggerated for clarity and is not to scale.

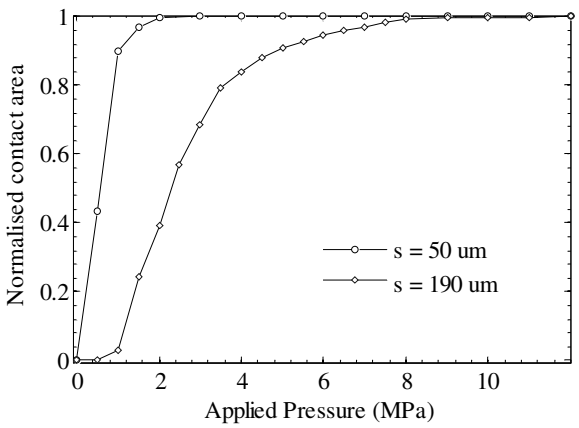


**Figure 5.** Simulated contact area as a function of applied pressure. For the range tested, no roof collapse occurs.

applied to the symmetry planes. The surround on part B is fixed to emulate the stamp when it is rigidly attached to the chuck. The simulated model is illustrated in figure 3, highlighting the relevant surfaces. The surfaces termed 'support' have the same depth as the print patterns and are included to avoid roof collapse. Further discussion regarding roof collapse and the role of the 'support' is provided in [33]. In figure 3, the stamp is subjected to a load of 20 MPa and is in contact with a surface (not shown) 190 $\mu$m above the initial position.

Both deformation without contact and deformation with contact to a surface at a flying height $s$ are simulated. Cross-sectional views of the membrane under different loads are illustrated in figure 4. The upper row illustrates free deformation whereas the lower row illustrates contact with a surface 190 $\mu$m above the stamp. Under free deformation, the print head does deform although much less than the membrane area, indicating that the stiffening of the print head is successful. In contact, the local stiffening is sufficient to avoid roof collapse. This conclusion is quantified in figure 5 which shows the variation of the contact area with applied load. Over the simulated range, no roof collapse occurred. When $s = 50$ $\mu$m, full contact is achieved very quickly ($\approx$2 MPa), whereas a load of $\approx$ 10 MPa is required for $s = 190$ $\mu$m.

Clearly, low operating pressures are desired to facilitate contact printing and minimize the risk of pattern deformation. Another reason is to avoid leaks at the interface between the membrane and the hydraulic chuck onto which the stamp is bonded. For example, the ultimate bond strength of plasma-bonded PDMS, which is a convenient method of assembling the hydraulic stamp, is of the order of 0.5 MPa [11, 38]. As shown in figure 5, one method of reducing the operating pressures is to use small flying height, but even with $s = 50$ $\mu$m the pressures required are higher than the ultimate bond strength of plasma-activated PDMS. Other methods of reducing the operating pressures would be to lower the stiffness of the membrane by, e.g., increasing the length of the membrane relative to the length of the print head, or reducing the thickness of the membrane. These aspects are beyond the scope of this paper but warrant further exploration.

## 3. Fabrication

In this section, replica moulding of the PDMS parts and stacking of the different layers are described. The fabrication of the silicon masters is first described, followed by the stamp casting process. Bonding of the different layers by using partially cured PDMS and assembly of the membrane to the hydraulic chuck are then presented.

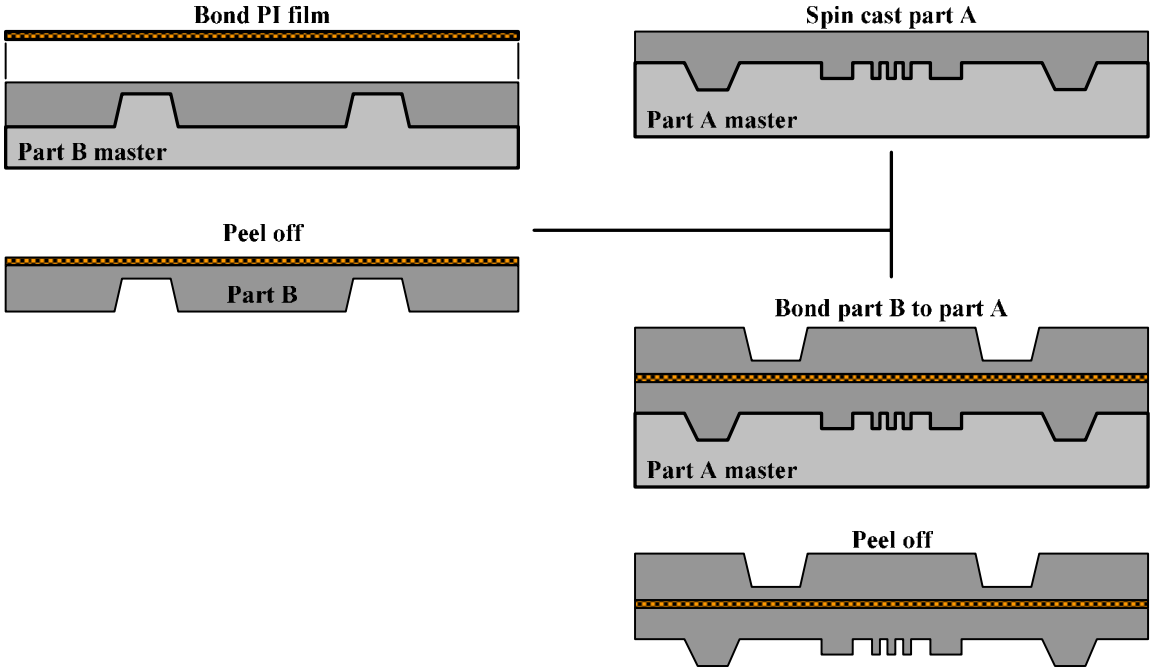


**Figure 6.** Moulding and stacking of PDMS parts with PI elastic backing.

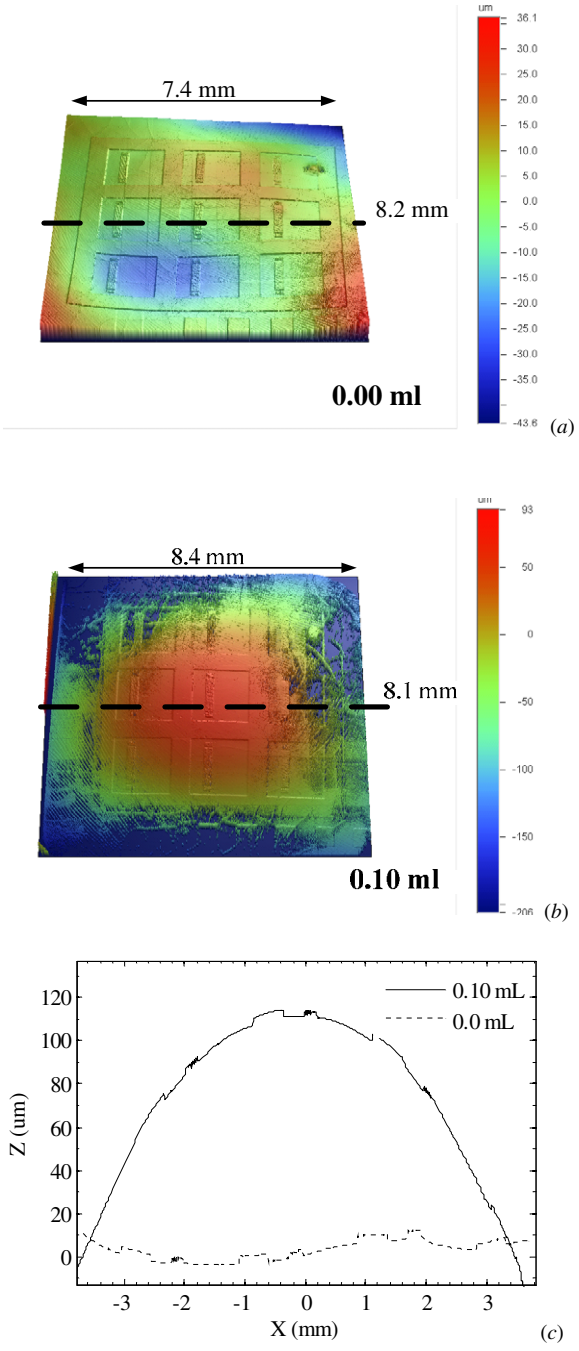


**Figure 7.** Optical interferometry images showing contour plots of the membrane with (*a*) 0.0 mL, (*b*) 0.10 mL injected volume. (*c*) The profile of the membrane in the centre.

### *3.1. Si master fabrication*

The masters used for moulding the PDMS parts are fabricated by conventional MEMS fabrication techniques presented in [33]. In each case, masters are formed from (1 0 0)-oriented Si. The part A master is formed using two-level lithography and etching, while the part B master is formed by single-level lithography and etching. For the part A master, the fine features are formed by lithography and RIE of the underlying substrate to a depth of ≈10 $\mu$m. The patterned substrate is then oxidized and subjected to a second lithography step to pattern the oxide. The oxide layer is then used as a mask for an anisotropic etch of the Si(1 0 0) to a depth of 200 $\mu$m using a KOH solution. The part B master is formed by oxidizing a Si(1 0 0) wafer and patterning the oxide layer by lithography and RIE. The latter is then used as a mask for an anisotropic etch, as with the part A master. Both masters are coated with a Teflon-like layer to facilitate demoulding.

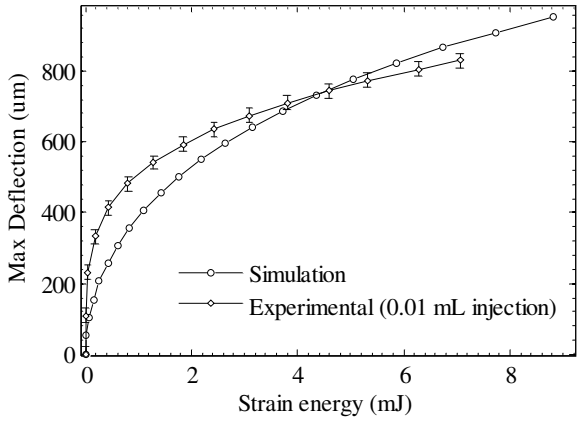


**Figure 8.** Comparison of simulated results with experimental result for the membrane under free deformation.

### *3.2. PDMS stamp casting and assembly*

This section describes the casting PDMS parts and their assembly. The PDMS parts are made of a 1:10 formulation of Sylgard 184 and the two parts are moulded separately on their respective masters and then bonded together, as shown in figure 6. A curing temperature of 90 °C is used throughout. Layers are glued together using a thin 30 $\mu$m thick partially cured PDMS layer. As shown in [38], partially cured PDMS exhibit higher bond strengths compared to plasma activated PDMS surfaces. In addition, for this device, some alignment is required and the partially cured adhesive allows adjustment even after initial contact has been made.

The casting and bonding process is shown in figure 6. Part B is spun cast and the PI film is attached using a partially cured adhesive layer. Part A is replica moulded in a similar manner to form an ∼200 $\mu$m thick layer. After cross-linking, a further ∼30 $\mu$m partially cured layer of PDMS is deposited as adhesive. The PI–part B assembly is peeled off from its master, turned upside down, aligned to part A and contacted. The stack is pressed together and cured on a hot plate at 90 °C for at least 1 h. After cross-linking, the finished stamp is finally peeled off from the master. Since the soft PDMS is always in bound by a rigid surface (either the Si master or the PI backing) no shrinkage is induced. Moreover, because of the quasi-symmetric structure, curling of the multilayer structure after release is minimized.

### *3.3. Bonding onto the hydraulic chuck*

The hydraulic chuck onto which the stamp is mounted is made out of 10 mm thick Perspex by precision machining. The square hydraulic cavity is formed using a computer

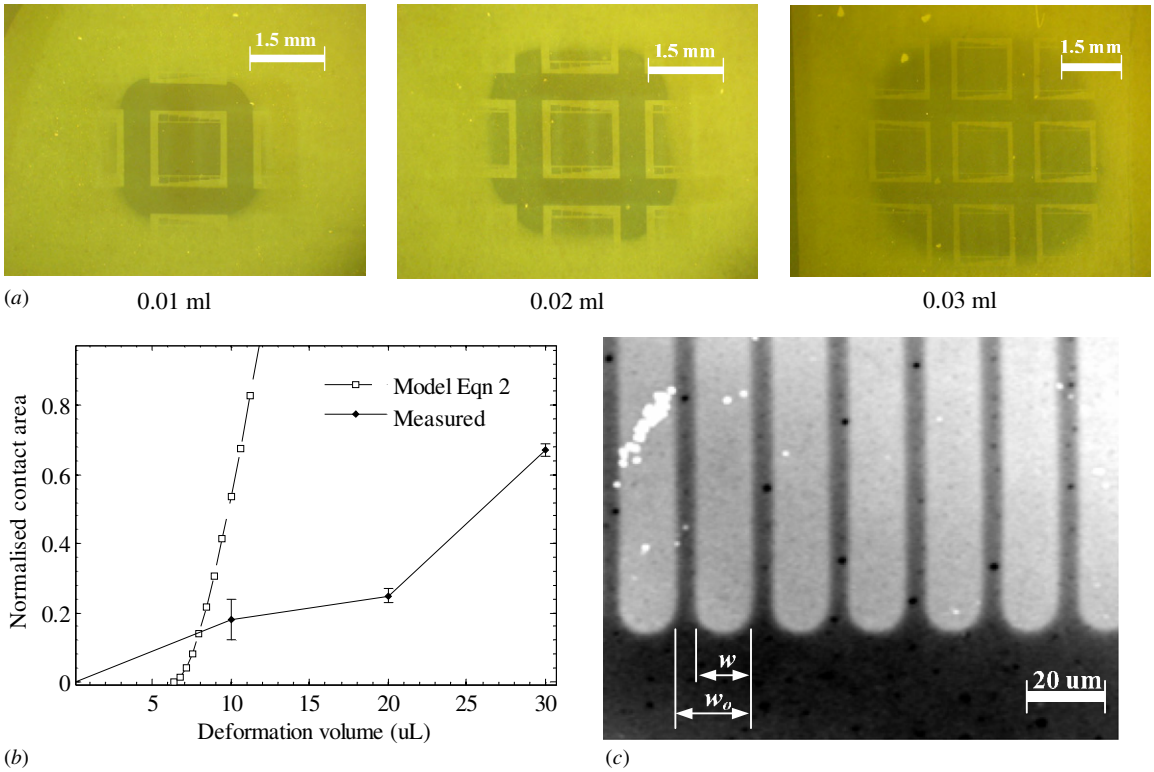


**Figure 9.** (*a*) Optical micrographs of Au (dark) patterns on glass (pale) formed by $\mu$CP with different volumes of hydraulic fluid. (*b*) Normalized contact area as a function of injected volume. The measured results indicate that a much larger injection is required to achieve contact. (*c*) Optical interferometer image (20× magnification) of the print with 0.02 mL showing accurate reproduction of features. Pale regions are Au, and dark regions are glass. $w$ denotes the line width, and $w_o$ the period.

controlled milling tool and the length of each side is 9 mm and corresponds to the size of the movable part of the stamp. Inlet and outlet ports connecting to the hydraulic chamber are drilled in from the sides and accommodate clear PTFE tubes (RS, rswww.com, #399-811) with bore diameter 1.01 mm and wall thickness 0.3 mm.

The PDMS stamp and the PTFE tubing were both bonded to the Perspex hydraulic chamber using a two-part epoxy glue (Araldite Precision). The tubing was fitted to the chuck and attached with epoxy polymer. The Perspex surface in contact with the stamp was roughened, cleaned and a thin layer of epoxy was applied to both the Perspex and the surround of part B on the stamp. The PDMS–PI assembly was aligned to the chuck, and gently pressed to make contact. An even weight was applied and the assembly was clamped together and allowed to cure at 20 °C for 48 h before any handling. The epoxy joints were reliable and no leakage was observed for the range tested. After curing and prior to printing, the substrate is placed on top of the spacer and held in place with an adjustable lid. The completed hydraulic $\mu$CP engine is illustrated in figure 1.

## 4. Experimental results and discussion

In this section, experiments are carried out on the hydraulic chuck and the results are presented. The pipes and the hydraulic chamber are first flushed by opening the tap on the outlet side and driving liquid through to minimize trapped air bubbles. The outlet tap is then closed and a known volume, $\Delta V$, is injected using a syringe driver (KDS 100, KD Scientific Inc.) at a flow rate of 2 mL $h^{-1}$. With a 5 mL or a 1 mL syringe, the smallest volume that can be injected is 0.01 mL.

### 4.1. Free deformation

In this section, the contact substrate and its support are removed and the unrestrained deformation of the square membrane is characterized. A known volume is injected, and the maximum vertical displacement at the centre of the stamp is measured using a microscope fitted with a Mitutoyo gauge.

In addition, the 2D areal metrology of the membrane under deformation was carried out using a white light interferometer (Wyko NT9100, Veeco Instruments Inc.). To enable reliable imaging, the substrate-facing side of the PDMS stamp was sputter coated with a 50 nm thick layer of Au to increase the reflectivity of the surface, prior to assembly. One issue is the restricted numerical aperture of the objective of the microscope, which limits the ability to capture data on sloping or curved edges. Contour maps of the membrane with no injected water and with 0.10 mL injection are illustrated in figures 7(*a*) and (*b*) while the cross-sectional profile of both is plotted on the same axes in figure 7(*c*) for comparison.

As shown in figure 7(*a*) the entire movable area of the stamp is reliably imaged whilst the lack of data points in the membrane region of figure 7(*b*) is due to the large slope. With 0.00 mL injection, the maximum height difference across the print head is ≈10 $\mu$m, whilst with an injection of 0.10 mL, the corresponding value is ≈140 $\mu$m. With no deformation,

the membrane has an estimated radius of curvature of ~120 mm, whilst with a deformation volume of 0.10 mL, the radius is ~40 mm.

The variation of the maximum deflection with injected volume is measured using the conventional microscope fitted with a height gauge. The maximum deflection initially rises very quickly with injected volume and the slope reduces as volume increases. The measured results were compared to the simulated model by relating the experimental data to the strain energy stored by the deformed membrane using equation (1). Strain energy, rather than injected volume was used as the former was more easily extracted from the CoventorWare software. Both plots are shown in figure 8 revealing good agreement between experiments and simulation.

### 4.2. Contact and $\mu$CP with a hydraulic drive

For $\mu$CP experiments, the stamp and substrates were arranged as in figure 1. The top face of the stamp was inked with 1-hexadecanethiol (as described in [33]), whilst the Au coated glass substrate was placed on the stamp spacer and held in position by the lid. In this configuration, the flying height, $s$, is 190 $\mu$m.

A known volume of water is injected and contact is maintained for 1 min. The outlet tap is then opened to retract the stamp and the substrate is replaced for another printing experiment. After printing, the Au coated substrate was etched in a ferricyanide solution (see [33]) to reveal the contacted area. The images formed after printing and etching are illustrated in figure 9. For the range of volumes tested, up to 70% of the total target area was contacted (see figures 9($a$) and ($b$)), and the parallel bars are successfully resolved with an injection of 0.02 mL (see figure 9($c$)).

As expected, the contact area increases with deformation volume. This trend is illustrated in figure 9($b$) where both experimental values and the trend predicted by the simplified model (equation (2)) are displayed. The volumes required to cause contact are significantly larger than those estimated. This is attributed to the presence of trapped air bubbles in the hydraulic cavity and pipes that are compressed as the pressure is increased. This volume is sufficiently compliant as to require injection of an additional volume of water.

### 4.3. $\mu$CP fidelity

Pattern fidelity was quantified by measuring the line width-to-period ($w/w_o$) ratio (see figure 9($c$)) of the printed images and comparing them with the stamp. The dimensions are obtained through high magnification (20×) interferometer images of the printed patterns and an example is shown in figure 9($c$). Nominally, the stamp has a $w/w_o$ value of 0.5, but, after processing and assembling, this ratio is measured to be 0.59 on the stamp. The variation of line width-to-period ratio with injected volume is plotted in figure 10($a$). For a 10 $\mu$L injection, the printed pattern closely matches the expected value, but the pattern quality degrades as larger volumes (and hence higher pressures) are injected. For a 30 $\mu$L deformation, the patterns widen significantly ($w/wo \approx$ 0.9) and the quality is poor.

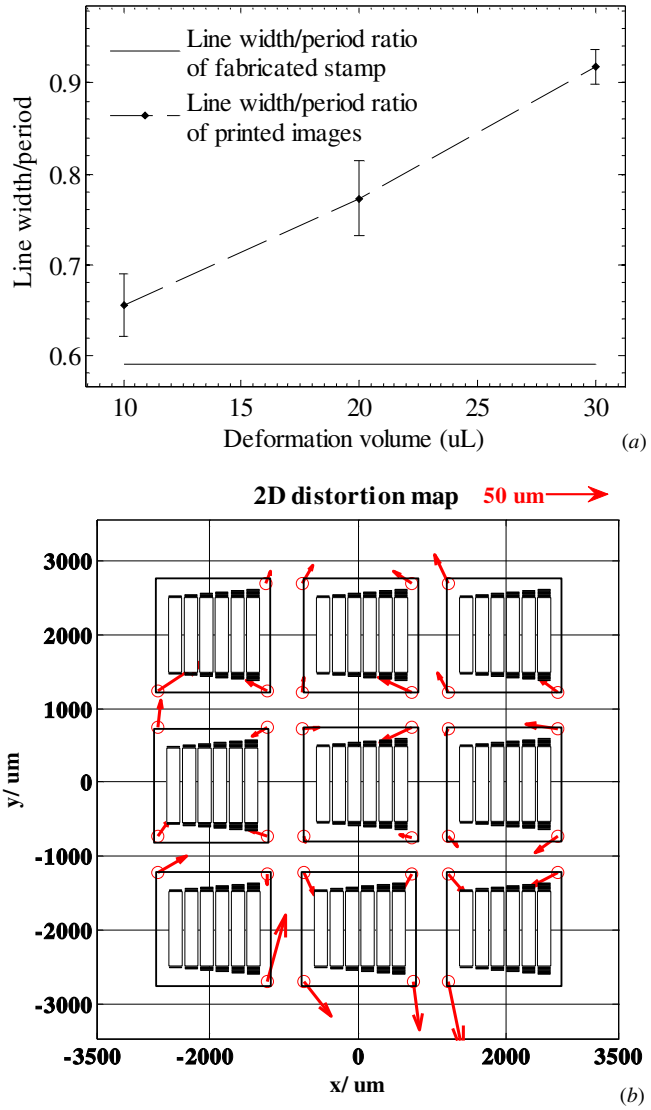


**Figure 10.** ($a$) Line width-to-period ratio ($w/w_o$) of printed images formed at different injection volumes. At larger volumes (hence, larger pressures) the line widths widen. ($b$) Distortion map showing the absolute distortion between the printed image and the fabricated stamp. The schematic shows the print pattern with the inner corners of the supporting bar marked by circles. The arrows (on a different scale) illustrate the direction and magnitude of the offset of the printed image with respect to the stamp.

In addition, the printing accuracy is characterized through a distortion map in figure 10($b$). Here, the printed pattern of figure 9($a$) with an injection of 0.03 mL is compared to the relief features on the PDMS stamp (see plan view of figure 2). The inner corners of the supporting bars are used as landmarks, and the relative offset at each corner is measured. The vector difference at each point is represented by arrows in figure 10($b$). The offsets are larger further from the centre and the maximum measured value is ≈50 $\mu$m.

### 4.4. Discussion

$\mu$CP with a hydraulic drive has successfully been demonstrated with the arrangement in figure 1. Image quality

is generally good; however, the arrangement suffers from a reduction in pattern fidelity as the hydraulic pressure is raised. This can be avoided by reducing the stiffness of the elastic membrane compared to that of the print head. For example, FEA of the stamp in figure 3 with the length of the membrane stretched by a factor of 2, $s = 190$ $\mu$m, and all other dimensions kept constant indicates that a pressure of 0.5 MPa is required for full contact compared to 10 MPa in the current arrangement. Additionally, the use of a more robust stamp material, such as in [14, 15], can improve relief feature stability, especially as resolution is driven to the nanoscale.

Lastly, the current system does have some restrictions in its controllability since the injected volume can only be controlled to the nearest 10 $\mu$L. This can be addressed by minimizing the hydraulic volume (e.g. with finer inlet/outlet tubes and a smaller hydraulic cavity) which would allow the use of a smaller syringe and hence reduce the smallest $\Delta V$. This would also reduce the volume of trapped air. Despite these shortcomings, the system provides a convincing proof of concept for hydraulically driven $\mu$CP and 10 $\mu$m wide patterns have successfully been transferred.

## 5. Conclusions

Hydraulically driven $\mu$CP has been proposed and demonstrated for the first time. The printing system comprises a replica-moulded tri-layered PDMS stamp bonded to a precision machined hydraulic chuck, and a substrate rigidly held at a calibrated height above the stamp. Accurate and controlled single-level $\mu$CP with a resolution of 10 $\mu$m has been achieved over areas up to 25 mm$^2$ although the pattern quality drops with increasing area.

The proposed method contributes to the field of $\mu$CP by providing a simple and accessible means of controlling the printing process. However, further work is required to reduce the distortion of the printed image relative to the original master, and the minimum feature size that can be reliably printed. One enhancement could be to increase the device size such that the membrane is less rigid and a smaller pressure is required to make contact.

Interesting questions are the compatibility of the hydraulic $\mu$CP system with nanoscale patterning and the possibility of multilevel patterning with different inks. As shown in [33], replication of 500 nm features on the PDMS stamp is feasible, and with a reduction in contact pressure, nanoscale patterning should be possible. Multilevel patterning could be carried out using localized inking with a corresponding inkwell, and printing using an independently addressable multi-cavity hydraulic system which would allow localized deflection of the membrane. The proposed method is suitable for biochemical patterning of substrates for fundamental studies of cell biology as well as for functionalizing devices (e.g. cantilever arrays) for sensor technologies.

## References


[1] Kumar A and Whitesides G M 1993 Features of gold having micrometer to centimeter dimensions can be formed through a combination of stamping with an elastomeric stamp and an alkanethiol 'ink' followed by chemical etching *Appl. Phys. Lett.* **63** 2002–4

[2] Xia Y and Whitesides G M 1998 Soft lithography *Angew. Chem. Int. Ed. Engl.* **37** 550–75

[3] Love J C, Estroff L A, Kriebel J K, Nuzzo R G and Whitesides G M 2005 Self-assembled monolayers of thiolates on metals as a form of nanotechnology *Chem. Rev.* **105** 1103–70

[4] Smith R K, Lewis P A and Weiss P S 2004 Patterning self-assembled monolayers *Prog. Surf. Sci.* **75** 1–68

[5] Whitesides G M, Ostuni E, Takayama S, Jiang X and Ingber D E 2001 Soft lithography in biology and biochemistry *Ann. Biomed. Eng.* **3** 335–73

[6] Bernard A, Renault J P, Michel B, Bosshard H R and Delamarche E 2000 Microcontact printing of proteins *Adv. Mater.* **12** 1067–70

[7] Lee J N, Park C and Whitesides G M 2003 Solvent compatibility of poly(dimethylsiloxane)-based microfluidic devices *Anal. Chem.* **75** 6544–54

[8] Delamarche E, Donzel C, Kamounah F S, Wolf H, Geissler M, Stutz R, Schmidt-Winkel P, Michel B, Mathieu H J and Schaumburg K 2003 Microcontact printing using poly(dimethylsiloxane) stamps hydrophilized by poly(ethylene oxide) silanes *Langmuir* **19** 8749–58

[9] Makamba H, Kim J H, Lim K, Park N and Hahn J H 2003 Surface modification of poly(dimethylsiloxane) microchannels *Electrophoresis* **24** 3607–19

[10] Owen M J and Smith P J 1994 Plasma treatment of polydimethylsiloxane *J. Adhes. Sci. Technol.* **8** 1063–75

[11] Bhattacharya S, Datta A, Berg J M and Gangopadhyay S 2005 Studies on surface wettability of poly(dimethyl) siloxane (PDMS) and glass under oxygen-plasma treatment and correlation with bond strength *J. Microelectromech. Syst.* **14** 590–7

[12] Jo B H, Van Lerberghe L M, Motsegood K M and Beebe D J 2000 Three-dimensional micro-channel fabrication in polydimethylsiloxane (PDMS) elastomer *J. Microelectromech. Syst.* **9** 76–81

[13] Delamarche E, Schmid H, Michel B and Biebuyck H 1997 Stability of molded polydimethylsiloxane microstructures *Adv. Mater.* **9** 741–6

[14] Schmid H and Michel B 2000 Siloxane polymers for high-resolution, high-accuracy soft lithography *Macromolecules* **33** 3042–9

[15] Odom T W, Love J C, Wolfe D B, Paul K E and Whitesides G M 2002 Improved pattern transfer in soft lithography using composite stamps *Langmuir* **18** 5314–20

[16] Burgin T, Choong V E and Maracas G 2000 Large area submicrometer contact printing using a contact aligner *Langmuir* **16** 5371–5

[17] Delamarche E, Vichiconti J, Hall S A, Geissler M, Graham W, Michel B and Nunes R 2003 Electroless deposition of Cu on glass and patterning with microcontact printing *Langmuir* **19** 6567–9

[18] Decre M M J, Schneider R M, Burdinski D, Schellekens J, Saalmink M and Dona R 2004 Wave printing (I): towards large-area, multilayer microcontact printing *Mater. Res. Soc. Symp. Proc.* **EXS-2** M4.9

[19] James C D 2000 Aligned microcontact printing of micrometer-scale poly-L-Lysine structures for controlled growth of cultured neurons on planar microelectrode arrays *IEEE Trans. Biomed. Eng.* **47** 17–21

[20] Chakra E B, Hannes B, Dilosquer G, Mansfield C D and Cabrera M 2008 A new instrument for automated microcontact printing with stamp load adjustment *Rev. Sci. Instrum.* **79** 064102

[21] GeSIM Micro-contact printing instruments http:www.gesim.de
[22] Syms R R A, Zou H, Choonee K and Lawes R A 2009 Silicon microcontact printing engines *J. Micromech. Microeng.* **19** 025027
[23] De Volder M and Reynaerts D 2010 Pneumatic and hydraulic microactuators: a review *J. Micromech. Microeng.* **20** 043001
[24] Oh K W and Ahn C H 2006 A review of microvalves *J. Micromech. Microeng.* **16** R13
[25] Laser D J and Santiago J G 2004 A review of micropumps *J. Micromech. Microeng.* **14** R35
[26] Moraes C, Sun Y and Simmons C A 2009 Solving the shrinkage-induced PDMS alignment registration issue in multilayer soft lithography *J. Micromech. Microeng.* **19** 065015
[27] Hoffman J M, Shao J, Hsu C H and Folch A 2004 Elastomeric molds with tunable microtopography *Adv. Mater.* **16** 2201–6
[28] Unger M A, Chou H-P, Thorsen T, Scherer A and Quake S R 2000 Monolithic microfabricated valves and pumps by multilayer soft lithography *Science* **288** 113–6
[29] Fredrickson C K 2004 Macro-to-micro interfaces for microfluidic devices *Lab Chip* **4** 526
[30] Yang Z 2002 A world-to-chip socket for microfluidic prototype development *Electrophoresis* **23** 3474
[31] Upchurch NanoPorts http:www.upchurch.com
[32] Bhagat A A S *et al* 2007 Re-usable quick-release interconnect for characterization of microfluidic systems *J. Micromech. Microeng.* **17** 42
[33] Choonee K and Syms R R A 2010 Multilevel self-aligned microcontact printing system *Langmuir* **26** 16163–70
[34] Fine R A and Millero F J 1973 Compressibility of water as a function of temperature and pressure *J. Chem. Phys.* **59** 5529–36
[35] Mark J 1999 *Polymer Data Handbook* (Oxford: Oxford University Press)
[36] Timoshenko S P and Woinowsky-Krieger S 1959 *Theory of Plates and Shells* 2nd edn (New York: McGraw-Hill)
[37] Senturia S D 2001 *Microsystem Design* (Boston: Kluwer)
[38] Eddings M A *et al* 2008 Determining the optimal PDMS–PDMS bonding technique for microfluidic devices *J. Micromech. Microeng.* **18** 067001